# In situ acoustic characterization of a locally reacting porous material by means of PU measurement and model fitting

Applied Acoustics 191 (2022) 108669

Contents lists available at ScienceDirect

Applied Acoustics

journal homepage: www.elsevier.com/locate/apacoust

Technical note

# In situ acoustic characterization of a locally reacting porous material by means of PU measurement and model fitting

Baltazar Briere de La Hosseraye *, Maarten Hornikx, Jieun Yang

*Department of the Built Environment, Eindhoven University of Technology, P.O. Box 513, 5600 MB Eindhoven, The Netherlands*

ARTICLE INFO

*Article history:*
Received 1 November 2021
Received in revised form 13 January 2022
Accepted 2 February 2022
Available online 24 February 2022

*2010 MSC:*
00-01
99-00

*Keywords:*
In situ measurements
Acoustic characterization
Model fitting
PU probe
Surface impedance
Absorption coefficient

ABSTRACT

Reliable data on acoustical properties of materials are crucial for the design of a desired acoustic environment as well as to obtain accurate results from acoustic simulations. Although the acoustical properties of materials can be obtained via laboratory measurements, situations where in situ measurements are needed are often encountered. However, in situ measurement methods presented so far are limited by their poor portability or inaccuracies in the low-frequency range. In this work, we propose a characterization method that combines an in situ pressure-velocity (PU) measurement with a model fitting procedure using the Delany-Bazley-Miki impedance model for porous materials. The method uses an optimization routine to find the best match of measured and modelled reflection coefficient values within a given frequency range for the optimization parameters: flow resistivity, panel thickness, and probe-sample distance. The optimal parameter values allow, in turn, calculating the porous panel's reflection coefficients for a broad frequency range including frequencies below the lower bounds of the optimization frequency range. The sensitivity of the method to panel width, lower bound of fitting frequency range, and to excluding parasitic reflections by time windowing is studied. The study shows that the proposed method provides characterization results in good agreement with reference data for panels of dimensions larger than 1800 mm and that the method is robust for reduction of one dimension of the panel down to 300 mm. It also shows that the model fitting accuracy is best when the frequency range of analysis is restricted to 1000–5000 Hz.



## 1. Introduction

Acoustical properties of materials are crucial aspects for controlling sound in an indoor environment. Particularly in room acoustics, the correct knowledge of material properties is of great importance when conducting room acoustic simulations to reproduce the acoustics of an existing space. Although a real-valued metric such as the absorption coefficient is sometimes sufficient to correctly simulate an absorbing surface, it is sometimes required to use complex-valued metrics, such as the surface impedance or the complex reflection coefficient to account for the phase shifts induced by the reflection of the sound waves on the surfaces.

To evaluate the complex reflection coefficient of a material by measurements, the standard procedure of the impedance tube method [1] is used, which allows estimating the complex surface impedance for normally incident sound waves. However, since the mounting and the material degradation can alter the acoustical properties of materials in situ, it would require the in situ sample to be brought to a laboratory and cut to fit in the tube. Because of that requirement, the impedance tube method can hardly be applied to estimate the acoustical properties of a material in situ.

To overcome this, efforts have been made to develop in situ characterization methods [2]. The advantage of such methods is significant: they do not require the destruction or the displacement of the sample. In situ measurement techniques can be categorized into approaches that use a microphone array [3–6], and approaches that use only a few measurement positions and are thus easily realisable with a single probe moved sequentially [7–13]. The former approaches use a large amount of microphones, for example 64 microphones (Ref. [4]) or 128 microphones (Ref. [5]), to reconstruct the sound field on the surface of the material, which in turn allows deducing the surface impedance. Because of the large number of microphone positions needed to reconstruct the sound field, however, such methods require either a long measurement time or a large number of channels, which reduces their practicality in the scope of in situ measurements.

Approaches that use only a few microphone positions require a sound field assumption, i.e., the sound field above the material's

* Corresponding author.
*E-mail address:* b.g.j.briere.de.la.hosseraye@tue.nl (B. Briere de La Hosseraye).

https://doi.org/10.1016/j.apacoust.2022.108669
0003-682X/

surface is assumed to resemble a known type of sound field. One simple approach is to assume that the sound field is a superposition of two plane waves travelling in-and-out of the material in opposite directions: the incident and reflected wave. More elaborate sound field models can be used, such as the image source method [14]. Using such a theoretical framework is advantageous because it allows for a measurement procedure with only a few microphone positions and a rapid processing based on the solving of a straightforward inverse problem. However, these approaches produce erroneous results in the low frequency range, where the sound field assumption typically does not hold. There also exist methods which take fully into account the spherical nature of the sound field [15,16]. These methods allow for more accurate results at low frequencies in exchange for a much higher mathematical complexity involving iterative algorithms. These methods were not considered in this work to keep the mathematical framework simple and because the success of the iterative algorithm would require a measurement accuracy that is challenging to reach in an actual in situ measurement situation.

Among the works using only a few measurement positions, de Bree et al. [7] introduced the pressure-velocity (PU) probe, that allows capturing the acoustic pressure and particle velocity at the same position. The PU measurement technique shows an greater stability of the results obtained to small sample sizes compared to both 2-pressure (PP) or 2-velocity (UU) techniques [17].

In this work, we propose a method to characterize a locally reacting porous material by combining a PU-based in situ measurement in normal incidence and a model fitting procedure based on the Delany-Bazley-Miki (DBM) impedance model for porous materials [18]. The model fitting finds the best matching prediction, for a given frequency range, between the measured complex reflection coefficient and the one predicted from the porous material model. The fitted model parameters, flow resistivity and thickness in the scope of the DBM model, are considered as the final results of the characterization. From this output, the reflection coefficient can be calculated using the DBM model in a broader frequency range, thus providing more reliable estimations in the low frequency range than would have been possible by a direct PU probe measurement.

This paper is organized as follows. In Section 2, the procedure of the proposed in situ characterization method is described in detail. Section 3 presents the experimental validation undertaken with the characterization of two rigidly backed porous panels. The thickness and flow resistivity extracted from the characterization are compared with measured data and the stability of the results is tested against different measurement configurations (various panel dimensions) and post-processing choices (frequency range of the fitting and amount of parasitic reflection energy in the signal) in order to evaluate its robustness and applicability in situ. Finally, Section 4 summarizes the paper and describes directions for future work.

## 2. In situ characterization procedure

Fig. 1 shows the outline of the proposed in situ characterization method. It relies essentially on two main steps: the in situ measurement itself and the model fitting of the data via an optimization routine. The details of the steps will be presented in the following Subsections 2.1 and 2.2.

### 2.1. In situ measurement

The measurement procedure revolves around the acquisition of 4 impulse responses (IRs). The acquisition of IRs has advantage over steady-state transfer functions in that it allows removing parasitic reflections (reflections from walls or ceiling of the measurement room) via time-windowing. At first, the pressure and the velocity in the direction of the source-probe axis have to be acquired in free field ($p_{ff}$ and $u_{ff}$ in Fig. 1), i.e., with the device away from any surfaces. These IRs are used to estimate the free field impedance $Z_{ff}$, which serves as a calibration value. Subsequently, the normal incidence pressure and velocity IRs are captured above the surface of the porous material in a similar way ($p$ and $u$ in Fig. 1), in order to yield an estimation of the impedance near the material $Z_m$. Fig. 2 shows the arrangement of sound source and PU probe above the surface of a porous panel of thickness $l$. The PU probe is placed above the material's surface at a distance $h$. The sound source is vertically aligned with the PU probe at a distance $d$.

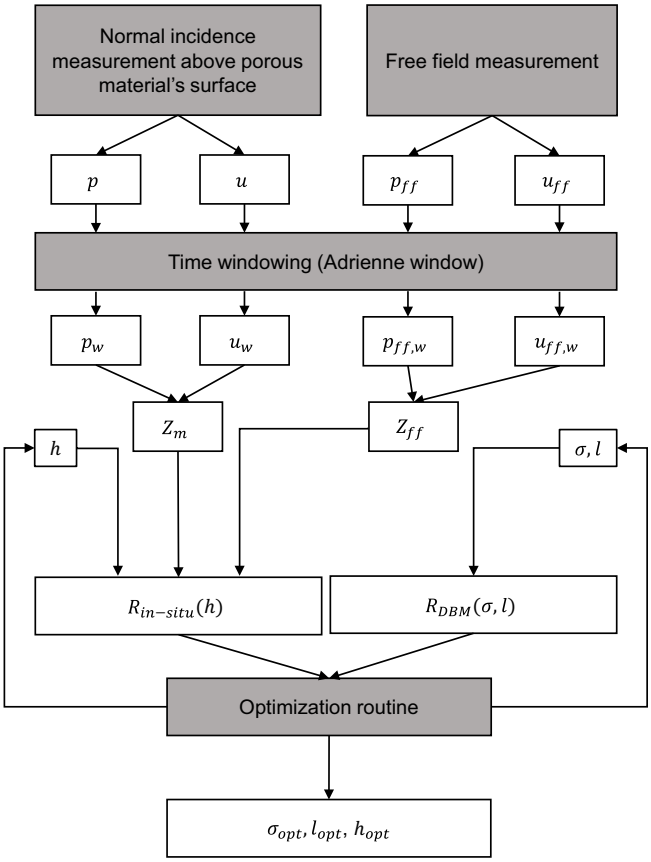


**Fig. 1.** Outline of the proposed in situ characterization method.

Fig. 3 shows a picture of the experimental setup used to capture the IRs. It makes use of the "In Situ Absorption setup" by Microflown Technologies, which was mounted on a lightweight tripod. This device consists of a PU probe attached to a small spherical loudspeaker via a structure that decouples vibrations between the loudspeaker and sensors. The PU probe is composed of an omnidirectional free field microphone and a bidirectional particle velocity sensor capturing the velocity along one single axis. The two sensors are very close to each other in the probe so that they are considered to be located at the same position. The decoupling structure sets the distance from the loudspeaker to the probe ($d$) to be 260 mm. The probe was oriented so that the velocity recorded was along the direction orthogonal to the panel's surface. The device was put in such a way that the source was vertically aligned with the sensor, so that the horizontal distance between the source and sensor is negligible and that the sound wave

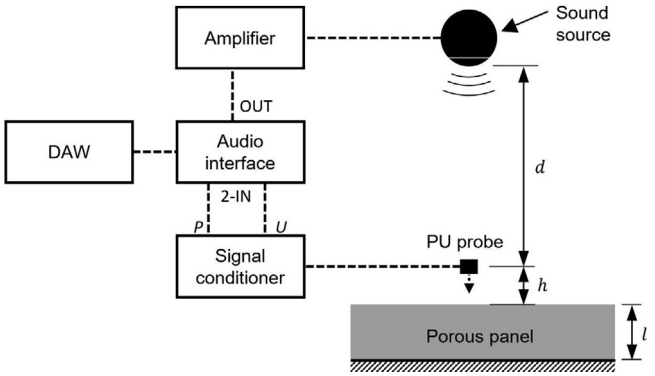


**Fig. 2.** Schematic of the measurement setup, with arrangement of the sound source and PU probe above a porous panel to measure $Z_m$. The horizontal distance between the source and the probe is considered negligible.

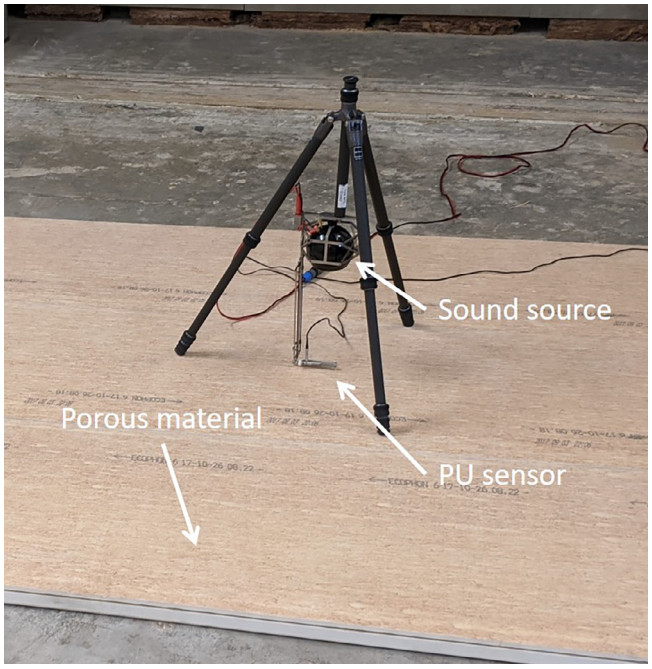


**Fig. 3.** Picture of measurement setup used for the experimental validation.

reaches the probe with normal incidence. The distance from the panel's surface to the probe ($h$) was targeted to lie below 20 mm, as recommended in Ref. [13]. The horizontal position of the probe was set to lie within the confidence region defined in Ref. [19], which is the region where the measured error resulting from wave diffraction from the panel's side edges are kept under control.

The output of the PU probe was connected to the Microflown's signal conditioner which separates the pressure and velocity signals into two channels. The outputs of the conditioner, as well as the loudspeaker, were connected to a 2-in 2-out USB audio interface (Triton V2 Standard, Acoustics Engineering), connected to a laptop running the Dirac 6 room acoustics acquisition software (Acoustics Engineering). The latter was used to perform the deconvolution of sent and recorded signals to derive the impulse responses for both pressure and velocity channels. The source signal, a 10 s-long exponential sine-sweep (ESS), was sent from Dirac 6 to the speaker via an intermediate amplifier. The distance from the source and receiver to the first reflective surface of the measurement room was around 1.5 m. The approximate time delay between the incident sound peak and the first parasitic reflections was thus computed as $\Delta t_{refl} = 7.4$ ms, and is used as a reference time-window length for which no parasitic reflection other than edge diffraction is present.

The four IRs obtained from the pressure and velocity signals are time-windowed using an Adrienne window [20]. The window is applied to the IRs such that the starting point of the flat portion of the window is set 0.2 ms before the initial peak, and the length of the time window adjusted to exclude the parasitic reflections from the analyzed signals using the previously calculated $\Delta t_{refl}$. An example of an Adrienne window is plotted along with an impulse response in Fig. 4. In Fig. 1, the four windowed IRs are denoted with an additional index $w$.

Subsequently, a Fourier transform is applied to the windowed signals and the complex reflection coefficient is calculated using the image source model presented in Refs. [10,21]. With known speaker-probe distance $d$ and probe-sample distance $h$, the complex reflection coefficient (using the $e^{+j\omega t}$ convention) can be written as

$$R_{insitu}(f,h) = \frac{\frac{Z_m}{Z_{ff}} - 1}{\frac{Z_m}{Z_{ff}}\left(\frac{d}{d+2h}\right)\left(\frac{jk(d+2h)}{jkd}\right) + 1}\left(\frac{d+2h}{d}\right)e^{2jkh}, \quad (1)$$

where $Z_m$ and $Z_{ff}$ are, respectively, the impedances (ratio of pressure over normal velocity spectra) captured near the material's surface and in the pseudo-free field situation, and $k = 2\pi f/c_0$ the wavenumber in air, with $f$ the frequency and $c_0$ the speed of sound in air. This formula relies on the assumption that both incident and reflected waves are plane waves but includes a correction for the amplitude decay of spherical sound waves [21].

### 2.2. Model fitting procedure

The reflection coefficient obtained from Eq. 1 depends on the probe-sample distance $h$. However, this parameter is hard to measure accurately in practice because the probe needs to be placed close to the measured surface ($< 20$ mm) [13], and the exact location of the acoustic center of the sensor can be subject to small deviations compared to its geometrical location, a problem reported for example in Ref. [9]. This is why, instead of treating the probe-sample distance as a fixed value obtained from a geometrical measurement, it was chosen to use it as an input variable of the model fitting procedure presented in this section.

The complex reflection coefficients acquired from the in situ measurements are fitted via an optimization routine to the ones

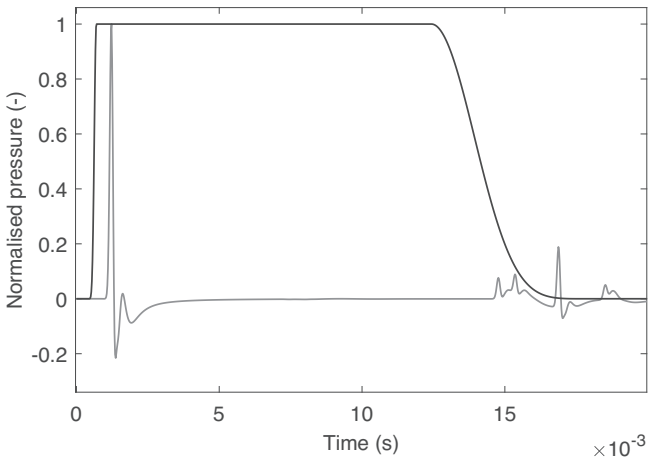


**Fig. 4.** Example of the time windowing of an impulse response (grey line) with the Adrienne window (black line).

predicted by the DBM model. In the DBM model, the material's propagation constant $k_c$ and characteristic impedance $Z_c$ are estimated through the following equations

$$k_c(f,\sigma) = \frac{2\pi f}{c_0}\left[1 + 7.81\left(10^3\frac{f}{\sigma}\right)^{-0.618} - j11.41\left(10^3\frac{f}{\sigma}\right)^{-0.618}\right], \quad (2)$$

$$Z_c(f,\sigma) = \rho_0 c_0\left[1 + 5.50\left(10^3\frac{f}{\sigma}\right)^{-0.632} - j8.43\left(10^3\frac{f}{\sigma}\right)^{-0.632}\right], \quad (3)$$

where $\sigma$ is the flow resistivity of the material and $\rho_0$ is the mass density of air. The normal incidence surface impedance of the porous material with a rigid backing $Z_{DBM}$ is then computed as

$$Z_{DBM}(f,\sigma,l) = -jZ_c\cot(k_c l), \quad (4)$$

with $l$ being the thickness of the sample. Then, the normal incidence complex reflection coefficient of the material $R_{DBM}$ is calculated as

$$R_{DBM}(f,\sigma,l) = \frac{Z_{DBM} - \rho_0 c_0}{Z_{DBM} + \rho_0 c_0}. \quad (5)$$

The DBM model needs only two input parameters, the flow resistivity and the thickness of the panel, to estimate the complex reflection coefficient. The reflection coefficient obtained by the DBM model, together with the reflection coefficient measured in situ (Eq. 1), is used to find optimal values for the probe-sample distance, flow resistivity and thickness of the panel.

By using Eqs. 1 and 5, a cost function $F$ is defined to minimize the absolute value of the difference between the frequency vectors of both imaginary and real parts of $R_{in-situ}(h)$ and $R_{DBM}(\sigma,l)$, which becomes

$$F(\sigma,l,h) = \sum_{f_l}^{f_u}||Re(R_{in-situ}(f,h) - R_{DBM}(f,\sigma,l))|| + \sum_{f_l}^{f_u}||Im(R_{in-situ}(f,h) - R_{DBM}(f,\sigma,l))||, \quad (6)$$

where $f_l$ and $f_u$ are the lower and upper bounds of the frequency range of the fitting ($\Delta_f$), respectively. We chose the reflection coefficient as the basis of the cost function because absolute values of both real and imaginary parts of the reflection coefficients are bounded by 1, which provides a natural normalization of deviations between the fittings of the real and imaginary parts during the optimization process. The frequency range of interest in this study is up to 5000 Hz. The lower bound of the frequency range is determined by the plane wave approximation used in Eq. 1, the type of source used in the setup and the source-to-probe distance. For the experimental setup used in this study, the assumption is valid down to around 500 Hz, as the wavelength below this frequency becomes large compared to the source-to-probe distance used (260 mm). Therefore, the reference frequency range of $\Delta f_{ref} = [500, 5000]$Hz is considered. The influence of the chosen frequency range on the results will be discussed in Section 3.3.

The cost function $F$ is minimized in MATLAB with the *fmincon* function used as the core solver to a *MultiStart* object, which runs the solver for a given number of starting points uniformly distributed across the search space, and yields the lowest minimum. The search space, which is defined by the lower ($x_l$) and upper boundaries ($x_u$) for each parameter, is presented in Table 1. The search space of the flow resistivity ($\sigma$) is chosen to encompass the values encountered for the most commonly used porous materials. The probe-to-sample distance ($h$) is expected to be within [0,30] mm. It should be noted that the thickness of the material ($l$) is considered as a variable in the characterization process in the same manner as the flow resistivity. This simulates a worst case scenario when it is not possible to measure the material thickness due to mounting conditions. In case the thickness can be measured as $l_{ref}$, the search boundaries can be narrowed to [0.95 $l_{ref}$, 1.05 $l_{ref}$], assuming that the thickness was measured with a 5% precision, while the search space of the other parameters remains the same. The number of starting points fed to the *Multistart* procedure $N_x$ was chosen as the lowest number ensuring no variation of the output parameters ($\sigma_{opt}$, $l_{opt}$ and $h_{opt}$) over 7 fittings based on the same experimental data. This number was experimentally derived as $N_x = 30$. For the fitting process, the reflection coefficients at 300 logarithmically spaced frequencies in the optimization frequency range were used.

**Table 1**
Lower ($x_l$) and upper limits ($x_u$) of search space for the optimization variables in this study.

| | Unknown thickness | | Known thickness | |
|---|---|---|---|---|
| | $x_l$ | $x_u$ | $x_l$ | $x_u$ |
| $\sigma$ (Pa · s/m$^2$) | $1 \times 10^3$ | $1 \times 10^6$ | $1 \times 10^3$ | $1 \times 10^6$ |
| $l$ (mm) | 0 | 200 | $0.95 \times l_{ref}$ | $1.05 \times l_{ref}$ |
| $h$ (mm) | 0 | 30 | 0 | 30 |

Based on this model fitting procedure, the final estimations of the measured and DBM-fitted reflection coefficients are extracted as

$$R_{in-situ,opt} = R_{in-situ}(h_{opt}), \quad (7)$$

$$R_{DBM,opt} = R_{DBM}(\sigma_{opt},\ l_{opt}). \quad (8)$$

Physically, $R_{DBM,opt}$ is the complex reflection coefficient obtained from the DBM-model parameters retrieved by the model fitting, and $R_{in-situ,opt}$ is the measured normal incidence complex reflection coefficient corrected with the probe-sample distance retrieved by model fitting. The measured and fitted model's normal incidence absorption coefficient can then be computed as

$$\alpha_{insitu,opt} = 1 - |R_{insitu,opt}|^2, \quad (9)$$

$$\alpha_{DBM,opt} = 1 - |R_{DBM,opt}|^2. \quad (10)$$

## 3. Experimental validation and discussion

### 3.1. Characterization samples

Fig. 5 shows pictures of the two materials, material A and B, used for the experimental validation. Material A comes in 40 mm-thick glass wool panels of dimensions 600 × 2700 mm. The panels have a thin (<1 mm) impervious coating glued to their front side, so the measurements were taken on the back of the panels to limit its potential influence. Three of these panels were assembled together into a greater surface of dimensions 1800 × 2700 mm, so as to create a larger sample for which size effect are negligible. Material B is a soft polyester wool coming in samples of dimensions 600 × 1200 mm. The panels thickness is about 100 mm. Likewise, the three panels were assembled to create a bigger panel of dimensions 1800 × 2400 mm. For all measurements, the samples were backed by a 300 mm-thick, smooth concrete floor in the workshop space of the acoustics laboratory of the Eindhoven University of Technology. Various objects and equipment were stored in the workshop space and surrounded the measurement location, but a clearance radius of approximately 1.5 m from the probe location was ensured.

**Fig. 5.** Picture of material A (left) and B (right).

The flow resistivities and thicknesses of the materials are presented in Table 2. The flow resistivity values were obtained from physical flow resistivity measurements provided by manufacturers. These values will be used to compare with the results from the proposed method in this paper.

### 3.2. Characterization results

Figs. 6 and 7 show measured and fitted complex reflection coefficients of materials A and B, respectively. For both materials, the measured and fitted reflection coefficients show good agreement in the fitting frequency range delimited with red-dashed lines in the figures. The discrepancies between the measured and fitted model's reflection coefficients are observed below $f_l$ (500 Hz). In this frequency range the product of the wavenumber by the source-to-probe distance *kd* is greater than 2.3 (value at 500 Hz), which suggests that the plane wave assumption does not hold because the probe is in the near field of the source at such low frequencies.

The retrieved flow resistivity, panel thickness, and probe-sample distance are shown in Table 3, as well as the final value of the cost function. The numbers in parentheses next to the retrieved values are relative errors with respect to the reference values presented in Table 2. For the probe-sample distance ($h_{opt}$), 15 mm was used as reference value, as it was the value measured when placing the probe above the samples. It is observed that in both unknown-thickness and known-thickness cases the retrieved thicknesses ($l_{opt}$) are smaller than the measured thicknesses. This can be partly explained by the characteristics of the materials. Material A features a thin coating on its front side and was measured on its backside. The presence of that thin layer of coating between the glass wool and the concrete slab might be responsible for this inaccuracy in thickness for material A. Material B does not have any coating but is a very soft material with a thickness varying slightly depending on the measurement point, which could contribute to an error in thickness. However, it is noticeable that even though the search space of the thickness is not constrained around the measured thickness, the retrieved thicknesses show accuracy within 15% deviation.

**Table 2**
The nominal flow resistivities $\sigma_{ref}$ and the thicknesses $l_{ref}$ of materials A and B.

| Sample | $\sigma_{ref}$ (kPa · s/m$^2$) | $l_{ref}$ (mm) |
|---|---|---|
| Material A | 82.2 | 40 |
| Material B | 3.9 | 100 |

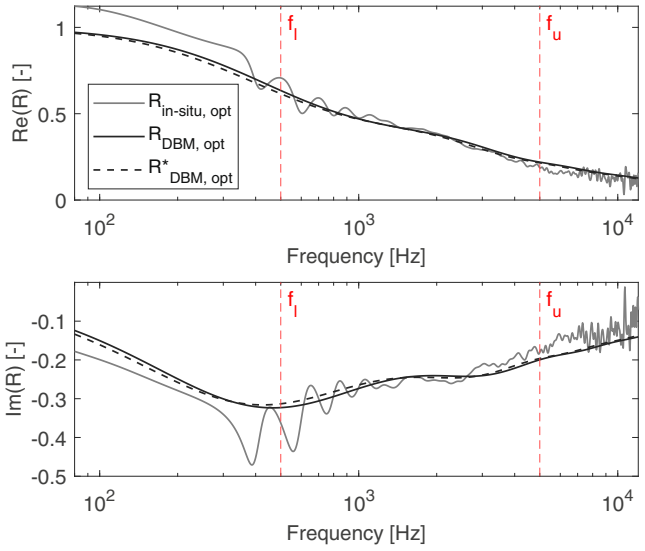


**Fig. 6.** The reflection coefficients of material A, measured ($R_{in-situ,opt}$), fitted with unknown thickness ($R_{DBM,opt}$) and fitted with known thickness ($R^*_{DBM,opt}$).

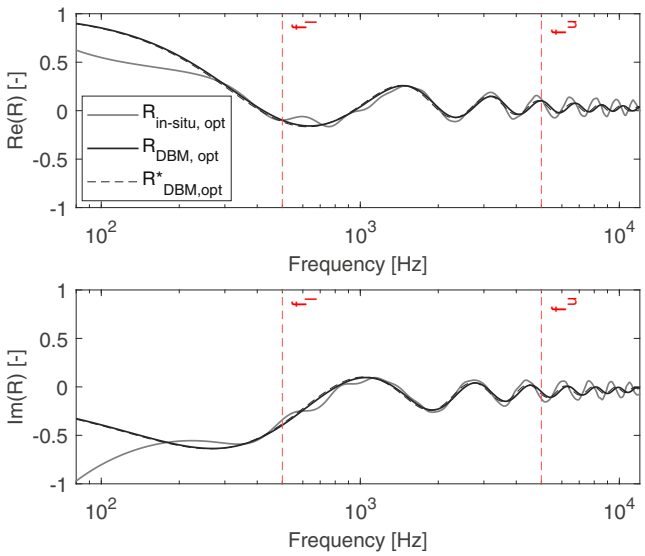


**Fig. 7.** The reflection coefficients of material B, measured ($R_{in-situ,opt}$), fitted with unknown thickness ($R_{DBM,opt}$) and fitted with known thickness ($R^*_{DBM,opt}$).

**Table 3**
Characterization results, in the case where the thickness is unknown and the case where it is known with a 5% precision. The deviation in percentage from the reference properties is shown in parenthesis.

| | Material A | Material B |
|---|---|---|
| Dimensions ($mm^3$) | 1800 × 2700 × 40 | 1800 × 2400 × 100 |
| | Unknown thickness | |
| $\sigma_{opt}$ (kPa·s/$m^2$) | 76.5 (−6.9%) | 5.2 (+33.3%) |
| $l_{opt}$ (mm) | 34.6 (−13.5%) | 93.5 (−7.5%) |
| $h_{opt}$ (mm) | 8.5 (−43.3%) | 11.1 (−32.7%) |
| $F(\sigma_{opt}, l_{opt}, h_{opt})$ (−) | 1.26 | 1.36 |
| | Known thickness | |
| $\sigma_{opt}$ (kPa·s/$m^2$) | 77.7 (−5.5%) | 4.7 (+20.5%) |
| $l_{opt}$ (mm) | 38.0 (−5.0%) | 95.0 (−5.0%) |
| $h_{opt}$ (mm) | 14.5 (−1.3%) | 13.8 (−8.0%) |
| $F(\sigma_{opt}, l_{opt}, h_{opt})$ (−) | 1.33 | 1.42 |

In the unknown thickness case, the flow resistivity estimation of material B shows a large relative error (+33.3%). However, the value of material B's flow resistivity is low, and the absolute difference is only 1.3 kPa·s/$m^2$. On the other hand, this can be related to the retrieved thickness. As the flow resistivity is the key parameter for sound dissipation in the porous medium, materials with low flow resistivity are more sensitive to the thickness, i.e., materials with low flow resistivity requires a longer sound path in the medium to absorb the same amount of sound energy compared to materials with high flow resistivity. Therefore, the underestimation of thickness, in turn, results in the large error in flow resistivity. This suggests that, without thickness constraints, the proposed method might estimate inaccurate flow resistivity in terms of relative error for porous materials with low flow resistivity.

Finally, it can be seen that using a tight constraint on the panel thickness (known thickness case) induces changes in the retrieved probe-sample distance. This is because the algorithm enforces an optimal fitting despite the constraints on $l$ by finding new optimal values for $h$.

Figs. 8 and 9 show the comparison of absorption coefficients obtained by using the retrieved DBM parameters ($\sigma_{opt}, l_{opt}$) and measured data in the frequency range 80–5000 Hz. The dotted lines labeled as reference are the absorption coefficients calculated with the values of nominal flow resistivity and thickness of materials A and B in Table 2. In these figures, it is observed that, similarly to the complex reflection coefficients, the absorption coefficients obtained from the proposed method are in good agreement with the ones measured within the fitting frequency range as well as with the reference data, in both unknown and known thickness settings. It can be seen that although the retrieved parameters are different depending on the thickness constraints, the deviations observed between the obtained absorption coefficients remain insignificant over the 80–5000 Hz frequency range. This indicates that for the sample measured, small variations in thickness would not alter the absorption coefficient significantly.

### 3.3. Sensitivity study

To investigate the robustness and limitations of the method, a sensitivity study of the characterization results was carried out against three independent parameters: panel width, model fitting's frequency range, and time window duration.

#### 3.3.1. Sensitivity to panel width

As evidenced in Ref. [22], the dimensions of the sample can have a significant influence on the measurement results because of diffracted waves at the sample's edges (which in this paper are considered separately from the parasitic reflections coming from the surfaces that are not part of the sample). The acquisition of the IRs was thus repeated for gradually reduced panel widths, down to 300 mm, to investigate the robustness of the method to samples of reduced size.

Tables 4 and 5 present the retrieved parameters from measurements on panels of decreasing widths for the two materials, for the unknown and known thickness cases. These tables display the deviations from the reference data in Table 2 as well as the deviations from acoustical properties calculated by the DBM model with the reference data. The metrics used are the relative error of flow resistivity ($\delta_\sigma$) and panel thickness ($\delta_l$) in regards to the reference values, average absolute deviations of real ($\Delta_R$) and imaginary part ($\Delta_I$) of reflection coefficients, and average absolute deviation of absorption coefficients ($\Delta_A$). The $\Delta_R, \Delta_I$, and $\Delta_A$ are obtained over the frequency range 80–5000 Hz to check the robustness of the results in the frequency range below $f_l$. As it does not relate to the properties of the material, the relative deviation in probe sample distance retrieved is omitted in this sensitivity study.

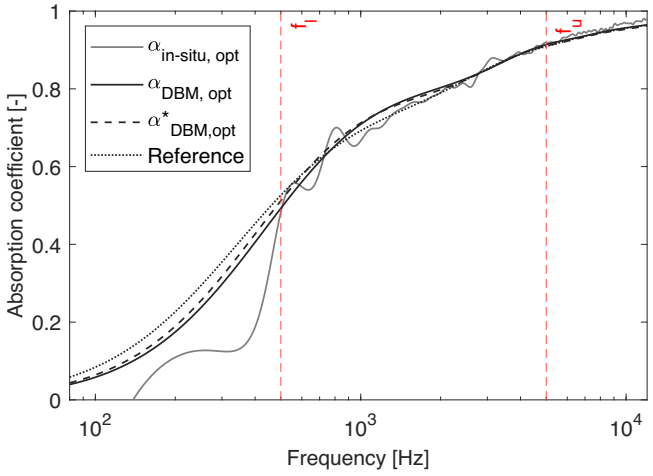


**Fig. 8.** Absorption coefficient of material A, measured ($\alpha_{in-situ,opt}$) and calculated using the retrieved DBM parameters ($\sigma_{opt}, l_{opt}$) in Table 3. $\alpha_{DBM,fit}$ and $\alpha^*_{DBM,fit}$ are the absorption coefficients calculated with the DBM parameters retrieved from the unknown and known thickness case, respectively.

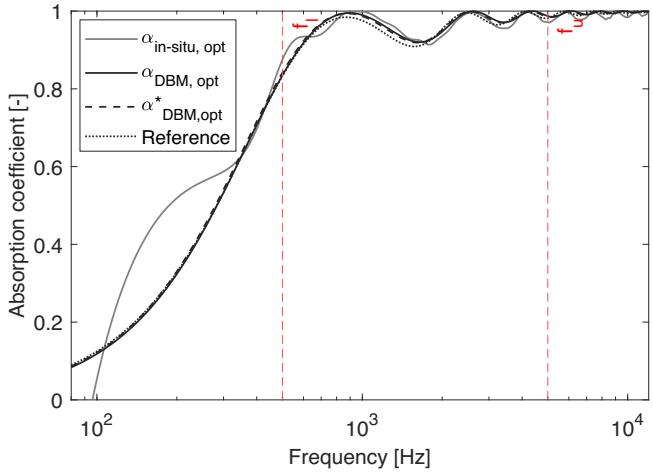


**Fig. 9.** Absorption coefficient of material B, measured ($\alpha_{in-situ,opt}$) and calculated using the retrieved DBM parameters ($\sigma_{opt}, l_{opt}$) in Table 3. $\alpha_{DBM,fit}$ and $\alpha^*_{DBM,fit}$ are the absorption coefficients calculated with the DBM parameters retrieved from the unknown and known thickness case, respectively.

**Table 4**
Characterization results for different panel widths of material A.

| | Unknown thickness | | | | Known thickness | | | |
|---|---|---|---|---|---|---|---|---|
| Panel width (mm) | 1800 | 1200 | 600 | 300 | 1800 | 1200 | 600 | 300 |
| $\sigma_{opt}$ (kPa·s/m$^2$) | 76.5 | 81.2 | 72.0 | 68.3 | 77.8 | 71.9 | 70.2 | 77.1 |
| $l_{opt}$ (mm) | 34.6 | 32.4 | 34.3 | 39.5 | 38.0 | 38.0 | 38.0 | 38.0 |
| $h_{opt}$ (mm) | 8.5 | 8.8 | 8.7 | 8.4 | 14.5 | 14.3 | 17.1 | 12.6 |
| $\delta_\sigma$ (%) | 6.7 | 1.0 | 12.2 | 16.7 | 5.1 | 12.3 | 14.3 | 6.0 |
| $\delta_l$ (%) | 13.5 | 19.0 | 14.2 | 1.3 | 5.0 | 5.0 | 5.0 | 5.0 |
| $\Delta_R$ (–) | 0.03 | 0.03 | 0.02 | 0.02 | 0.04 | 0.03 | 0.03 | 0.03 |
| $\Delta_I$ (–) | 0.02 | 0.02 | 0.01 | 0.01 | 0.02 | 0.02 | 0.02 | 0.02 |
| $\Delta_A$ (–) | 0.03 | 0.02 | 0.02 | 0.01 | 0.03 | 0.02 | 0.02 | 0.02 |

**Table 5**
Characterization results for different panel widths of material B.

| | Unknown thickness | | | | Known thickness | | | |
|---|---|---|---|---|---|---|---|---|
| Panel width (mm) | 1800 | 1200 | 600 | 300 | 1800 | 1200 | 600 | 300 |
| $\sigma_{opt}$ (kPa·s/m$^2$) | 5.2 | 5.3 | 5.2 | 6.0 | 4.8 | 4.7 | 4.8 | 5.1 |
| $l_{opt}$ (mm) | 93.5 | 93.5 | 94.6 | 89.3 | 95.0 | 95.0 | 95.0 | 95.0 |
| $h_{opt}$ (mm) | 11.1 | 11.1 | 12.1 | 12.7 | 13.8 | 10.7 | 15.6 | 7.6 |
| $\delta_\sigma$ (%) | 33.3 | 35.9 | 33.3 | 53.8 | 23.0 | 20.5 | 23.0 | 30.9 |
| $\delta_l$ (%) | 15.0 | 15.0 | 14.0 | 18.8 | 5.0 | 5.0 | 5.0 | 5.0 |
| $\Delta_R$ (–) | 0.06 | 0.05 | 0.03 | 0.06 | 0.03 | 0.03 | 0.03 | 0.03 |
| $\Delta_I$ (–) | 0.06 | 0.05 | 0.03 | 0.06 | 0.03 | 0.03 | 0.03 | 0.03 |
| $\Delta_A$ (–) | 0.01 | 0.01 | 0.01 | 0.01 | 0.01 | 0.01 | 0.01 | 0.01 |

The results show that the size of the panel does not influence significantly the characterization result. In the unknown thickness case, a slight increase of the flow resistivity error is observed for 300 mm wide panels for panel B, but this error only results in small deviations in the reflection coefficient. The results also show that in the known thickness case for material A, the smallest sample provides a more accurate retrieval of the material resistivity, whereas some increase in deviation would have been expected due to the increased influence of edge diffraction for smaller samples. The reason for this is not clear. This could be because the constrained thickness in the model fitting induces error in the flow resistivity retrieval, which could then compensate the error originating from the finite size in the case of the smallest sample. It is also possible that the probe happened to be positioned in a spot where the waves diffracted from both opposite edges of the sample cancel each other out, thereby resulting in an error smaller than in the case of the larger samples. It should be noted that two choices made in this study are inherently reducing the potential impact of the size of the panels: (1) the PU probe is located within the confidence regions of the panels for PU probe measurement so that the error related to edge diffraction is kept under control, (2) only the reduction of one dimension of the panels is considered. If the PU probe were located near the edges of the panel or if the panel's dimension were made even smaller, the error would increase.

### 3.3.2. Sensitivity to model fitting's frequency range

The frequency range of the model fitting ($\Delta f = [f_l, f_u]$) can influence the accuracy of the results, as the variations of the reflection coefficient over frequency is a key input to the model fitting process. Because the measurement procedure relies on an approximation which is valid above 500 Hz, only the lower frequency limit $f_l$ is changed while the upper limit is fixed to $f_u$ = 5000 Hz. Thus, $f_l$ is varied by increments of one octave bands from 125 Hz to 1 kHz.

In Tables 6 and 7 the results with varying $f_l$ are presented. It can be seen that including lower frequencies (results with $f_l = 125$ Hz and $f_l = 250$ Hz) slightly deteriorates the agreement of the retrieved parameters with the reference, for both materials and both sets of thickness constraints. On the contrary, removing frequencies below 1000 Hz from the analysis improves the accuracy of the characterization. This is due to the fact that Eq. 1, which uses a plane wave incidence assumption, is much more accurate at higher frequencies than at lower frequencies.

**Table 6**
Characterization results of material A for different $f_l$.

| | Unknown thickness | | | | Known thickness | | | |
|---|---|---|---|---|---|---|---|---|
| $f_l$ (Hz) | 125 | 250 | 500 | 1000 | 125 | 250 | 500 | 1000 |
| $\sigma_{opt}$ (kPa·s/m$^2$) | 71.0 | 71.3 | 76.5 | 78.7 | 67.0 | 70.7 | 77.8 | 80.2 |
| $l_{opt}$ (mm) | 30.9 | 31.6 | 34.6 | 38.8 | 38.0 | 38.0 | 38.0 | 42.0 |
| $h_{opt}$ (mm) | 14.8 | 14.9 | 15.1 | 15.2 | 13.9 | 14.1 | 14.5 | 14.5 |
| $\delta_\sigma$ (%) | 13.4 | 13.0 | 6.7 | 4.0 | 18.3 | 13.8 | 5.1 | 2.3 |
| $\delta_l$ (%) | 22.8 | 21.0 | 13.5 | 3.0 | 5.0 | 5.0 | 5.0 | 5.0 |
| $\Delta_R$ (–) | 0.02 | 0.02 | 0.03 | 0.01 | 0.03 | 0.03 | 0.03 | 0.005 |
| $\Delta_I$ (–) | 0.02 | 0.02 | 0.02 | 0.004 | 0.02 | 0.02 | 0.03 | 0.003 |
| $\Delta_A$ (–) | 0.02 | 0.02 | 0.03 | 0.004 | 0.02 | 0.02 | 0.01 | 0.004 |

### 3.3.3. Sensitivity to parasitic reflection

If the time window is too long, the presence of parasitic reflections from the measurement's environment can distort the spectra of the measured reflection coefficients. The parasitic reflections considered in this section do not include the sound diffracted on the edges of the sample itself, but only the ones coming from the surrounding objects. However, during the time-windowing step, it may not be straightforward to locate exactly unwanted reflections as they are of small amplitude, and thus it is not straightforward to set the ideal window length. Therefore, it is of interest to study whether the inclusion of late parasitic reflections influences the characterization.

The amount of parasitic reflection in the windowed signal was assessed by computing a late reflection ratio (*LRR*) of the windowed signal

$$LRR = 20\log_{10}\left(\frac{||p_{w,early}||}{||p_w||}\right), \quad (11)$$

where $||p_{w,early}||$ is the total amplitude of the 'clean' widowed time signal, including only the incident sound wave and the sound wave reflected from the material, and $||p_w||$ is the total amplitude of the whole windowed time signal, including potential parasitic reflections. Thus, if all the parasitic reflections are windowed out *LRR* is equal to 0, and is negative otherwise. The time marking the limit of the 'clean' part of the signal was determined based on the distance from the probe to the nearest reflective surface that is not the material under study. Results of the characterization were then obtained for various time window durations corresponding to various *LRR* values.

The results shown in Tables 8 and 9 show that the late parasitic reflections have a very limited impact on the results of the characterizations: the deviations from the reference appear stable to the presence of late parasitic reflection, even when the presence of multiple parasitic reflections in the signal is clearly indicated by deformations of the measured spectra. This is displayed in the case with $t_{win} = 85$ ms (material A) in Fig. 10. These results imply that including late parasitic reflections into the analysed signal does not influence much the result of the characterization even for $LRR < -3$ dB. This result should be linked to the conditions of the measurements, where the nearest reflective object was located about 1.5 m from the receiver location, while the sound source was only 260 mm away. If the source was located further away

**Table 7**
Characterization results of material B for different $f_l$.

| | Unknown thickness | | | | Known thickness | | | |
|---|---|---|---|---|---|---|---|---|
| $f_l$ (Hz) | 125 | 250 | 500 | 1000 | 125 | 250 | 500 | 1000 |
| $\sigma_{opt}$ (kPa·s/m$^2$) | 5.4 | 5.3 | 5.2 | 4.2 | 4.9 | 4.7 | 4.8 | 4.1 |
| $l_{opt}$ (mm) | 91.2 | 92.1 | 93.5 | 96.4 | 95.0 | 95.0 | 95.0 | 97.1 |
| $h_{opt}$ (mm) | 8.4 | 10.1 | 11.1 | 11.1 | 11.3 | 10.8 | 13.8 | 10.7 |
| $\delta_\sigma$ (%) | 38.5 | 35.9 | 33.3 | 7.7 | 25.6 | 20.5 | 23.1 | 5.1 |
| $\delta_l$ (%) | 17.1 | 16.3 | 15.0 | 12.4 | 5.0 | 5.0 | 5.0 | 2.9 |
| $\Delta_R$ (–) | 0.06 | 0.06 | 0.06 | 0.03 | 0.03 | 0.03 | 0.03 | 0.03 |
| $\Delta_I$ (–) | 0.06 | 0.06 | 0.06 | 0.03 | 0.03 | 0.03 | 0.03 | 0.03 |
| $\Delta_A$ (–) | 0.01 | 0.01 | 0.01 | 0.004 | 0.005 | 0.004 | 0.004 | 0.003 |

**Table 8**
Characterization results of material A for different time-window lengths ($t_{win}$).

| | Unknown thickness | | | | | Known thickness | | | | |
|---|---|---|---|---|---|---|---|---|---|---|
| $t_{win}$ (ms) | 7.5 | 21.0 | 45.0 | 85.0 | 130.0 | 7.5 | 21.0 | 45.0 | 85.0 | 130.0 |
| *LRR* (dB) | 0.0 | −0.5 | −1.1 | −2.3 | −3.3 | 0.0 | −0.5 | −1.1 | −2.3 | −3.3 |
| $\sigma_{opt}$ (kPa·s/m$^2$) | 76.5 | 75.1 | 75.2 | 74.7 | 75.0 | 77.8 | 77.6 | 77.8 | 77.4 | 77.1 |
| $l_{opt}$ (mm) | 34.6 | 34.3 | 34.2 | 34.4 | 34.3 | 38.0 | 38.0 | 38.0 | 38.0 | 38.0 |
| $h_{opt}$ (mm) | 15.1 | 15.2 | 15.2 | 15.1 | 15.1 | 14.5 | 14.5 | 14.5 | 14.5 | 14.6 |
| $\delta_\sigma$ (%) | 6.7 | 8.4 | 8.3 | 8.9 | 8.5 | 5.1 | 5.4 | 5.1 | 5.6 | 6.0 |
| $\delta_l$ (%) | 13.5 | 14.3 | 14.5 | 14.0 | 14.3 | 5.0 | 5.0 | 5.0 | 5.0 | 5.0 |
| $\Delta_R$ (–) | 0.03 | 0.03 | 0.02 | 0.02 | 0.01 | 0.02 | 0.02 | 0.02 | 0.02 | 0.02 |
| $\Delta_I$ (–) | 0.02 | 0.02 | 0.01 | 0.01 | 0.01 | 0.01 | 0.01 | 0.01 | 0.01 | 0.01 |
| $\Delta_A$ (–) | 0.03 | 0.02 | 0.01 | 0.01 | 0.01 | 0.01 | 0.01 | 0.01 | 0.01 | 0.01 |

**Table 9**
Characterization results of material B for different time-window lengths ($t_{win}$).

| | Unknown thickness | | | | | Known thickness | | | | |
|---|---|---|---|---|---|---|---|---|---|---|
| $t_{win}$ (ms) | 7.2 | 23.0 | 47.0 | 62.0 | 84.0 | 7.2 | 23.0 | 47.0 | 62.0 | 84.0 |
| *LRR* (dB) | 0.0 | −0.5 | −1.2 | −2.3 | −3.3 | 0.0 | −0.5 | −1.2 | −2.3 | −3.3 |
| $\sigma_{opt}$ (kPa·s/m$^2$) | 5.2 | 5.0 | 5.1 | 5.1 | 5.0 | 4.8 | 4.8 | 4.8 | 4.8 | 4.8 |
| $l_{opt}$ (mm) | 93.5 | 93.8 | 94.1 | 94.3 | 94.1 | 95.0 | 95.0 | 95.1 | 95.4 | 95.6 |
| $h_{opt}$ (mm) | 11.1 | 11.0 | 11.0 | 11.1 | 11.2 | 13.8 | 10.5 | 10.1 | 9.8 | 9.6 |
| $\delta_\sigma$ (%) | 33.3 | 28.2 | 30.7 | 30.7 | 28.2 | 23.1 | 23.1 | 23.1 | 23.1 | 23.1 |
| $\delta_l$ (%) | 15.0 | 14.7 | 14.5 | 14.3 | 14.5 | 5.0 | 5.0 | 4.9 | 4.6 | 4.4 |
| $\Delta_R$ (–) | 0.06 | 0.05 | 0.04 | 0.04 | 0.04 | 0.03 | 0.03 | 0.03 | 0.03 | 0.03 |
| $\Delta_I$ (–) | 0.06 | 0.05 | 0.04 | 0.04 | 0.03 | 0.03 | 0.03 | 0.03 | 0.03 | 0.03 |
| $\Delta_A$ (–) | 0.01 | 0.007 | 0.005 | 0.004 | 0.005 | 0.004 | 0.004 | 0.004 | 0.004 | 0.004 |

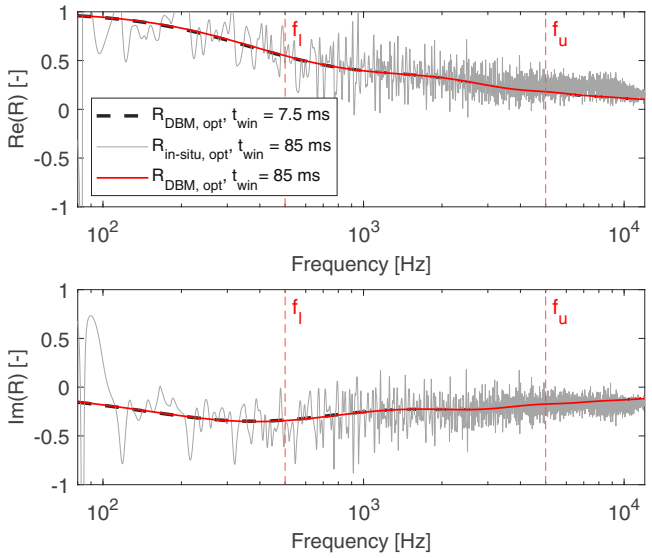


**Fig. 10.** Comparison of model-fitted reflection coefficients obtained from measurements with multiple late parasitic reflections included in the signal ($t_{win} = 85$ ms) with the ones without parasitic reflection ($t_{win} = 7.5$ ms) for material A. The measured reflection coefficient with multiple late parasitic reflections is also shown. The fitted model derived from the signal with many parasitic reflections deviates very slightly from the model derived from the signal without parasitic reflections.

or the reflective surfaces located closer, the influence of the parasitic reflections would be expected to increase.

## 4. Conclusion

In this study, the inverse characterization of porous materials from in situ PU measurement, assuming a locally reacting behavior, is proposed. The method aims at providing a simple and robust means to characterize a porous material of unknown properties encountered in situ. The procedure relies on two steps: (i) the acquisition of pressure and particle velocity IRs to measure the complex reflection coefficients of materials and (ii) a model fitting optimization routine, minimizing the difference between the measured reflection coefficient and the one obtained from the Delany-Bazley-Miki model for porous materials in the frequency range $\Delta f = [500, 5000]$ Hz.

The proposed characterization method performed on large samples provided results in good agreement with reference data for two porous materials of different flow resistivities and thicknesses. The results showed that the thickness was underestimated by $13 - 15\%$ and that the flow resistivity of the porous material with a high flow resistivity (material A, 82.2 kPa.s/m$^2$) was estimated with a 6.9% error and a low flow resistivity (material B, 3.9 kPa.s/m$^2$) with a 33.3% error. However, these errors were reduced when an 5% precise estimation of the thickness was assumed and the routine's search boundaries modified accordingly. In that case, the deviation of the retrieved flow resistivity remained within 5.5% (material A) and 20.5% (material B). The errors in percentage of material B are large but the absolute difference of the flow resistivity is within 1.5 kPa.s/m$^2$. Despite these deviations, the DBM modelled complex reflection coefficients and absorption coefficients obtained using the retrieved parameters from both unknown and known thickness fitting were in very close agreement over a broad frequency range [80, 5000] Hz.

Furthermore, a sensitivity study related to the panel width, the choice of the fitting frequency range, and late parasitic reflection was performed. Results showed that, for the locations of the probe and source used in this study, the procedure is robust to the reduction of one single dimension of the sample down to 300 mm, with a maximum deviation in terms of the fitted model's absorption coefficient below 0.06. It was also shown that the fitting frequency range did affect the outcome of the characterization, as a slightly better agreement with reference values was obtained by restricting it to the higher frequencies ($\Delta f = [1000, 5000]$ Hz). Finally, it was observed that the procedure was robust to the presence of late parasitic reflections even when the total late reflection energy was approximately equal to the early sound energy.

As the presented method focuses on the characterization of a porous absorber backed by a hard wall, it is also of interest to investigate if the method can be adapted to characterize more complex sound absorbing systems such as suspended ceilings, porous materials with impervious covers or acoustic carpets.

## CRediT authorship contribution statement

**Baltazar Briere de La Hosseraye:** Conceptualization, Methodology, Software, Validation, Formal analysis, Investigation, Writing – original draft, Visualization, Data curation. **Maarten Hornikx:** Resources, Writing – review & editing, Supervision, Project administration, Funding acquisition, Formal analysis, Conceptualization, Visualization. **Jieun Yang:** Writing – review & editing, Supervision, Conceptualization, Formal analysis, Visualization.

## Declaration of Competing Interest

The authors declare the following financial interests/personal relationships which may be considered as potential competing interests: Baltazar Briere de La Hosseraye reports financial support was provided by the European Union's Horizon 2020 research and innovation programme.

## Acknowledgements

This project has received funding from the European Union's Horizon 2020 research and innovation programme under the Marie Sklodowska-Curie grant agreement number 721536.

## References

[1] ISO 10534-2. Acoustics – Determination of sound absorption coefficient and impedance in impedance tubes – Part 2: Transfer-function method. International Organization for Standardization: Geneva, Switzerland.
[2] Brandão E, Lenzi A, Paul S. A review of the in situ impedance and sound absorption measurement techniques. Acta Acust United Acustica 2015;101(3):443–63.
[3] Tamura M, Allard JF, Lafarge D, Cedex LM. Spatial Fourier-transform method for measuring reflection. J Acoust Soc Am 1995;97(4):2255–62.
[4] Richard A, Fernandez-Grande E, Brunskog J, Jeong C-H. Estimation of surface impedance at oblique incidence based on sparse array processing. J Acoust Soc Am 2017;141(6):4115–25.
[5] Hald J, Song W, Haddad K, Jeong C-H, Richard A. In-situ impedance and absorption coefficient measurements using a double-layer microphone array. Appl Acoust 2019;143:74–83.
[6] Nolan M. Estimation of angle-dependent absorption coefficients from spatially distributed in situ measurements. J Acoust Soc Am 2020;147(2). EL119–EL124.
[7] de Bree H-E, Lanoye R, De Cock S, van Heck J. In situ, broad band method to determine the normal and oblique reflection coefficient of acoustic materials. SAE Technical Papers 724.
[8] Li J-F, Hodgson M. Use of pseudo-random sequences and a single microphone to measure surface impedance at oblique incidence. J Acoust Soc Am 1997;102(4):2200–10.
[9] Brandão E, Flesch RCC, Lenzi A, Flesch CA. Estimation of pressure-particle velocity impedance measurement uncertainty using the Monte Carlo method. J Acoust Soc Am 2011;130(1). EL25–EL31.
[10] Li M, van Keulen W, Tijs E, van de Ven M, Molenaar A. Sound absorption measurement of road surface with in situ technology. Appl Acoust 2015;88:12–21.
[11] Sakamoto N, Otsuru T, Tomiku R, Yamauchi S. Reproducibility of sound absorption and surface impedance of materials measured in a reverberation

room using ensemble averaging technique with a pressure-velocity sensor and improved calibration. Appl Acoust 2018;142:87–94.
[12] Müller-Trapet M, Dietrich P, Aretz M, van Gemmeren J, Vorländer M. On the in situ impedance measurement with pu-probes — Simulation of the measurement setup. J Acoust Soc Am 134.
[13] Pedrero A, Navacerrada MA, Prida DD, Iglesias L, Díaz-Chyla A. On the accuracy of the sound absorption measurement with an impedance gun. Appl Acoust 2020;158:107039.
[14] Li J, Hodgson M. Use of pseudo-random sequences and a single microphone to measure surface impedance at oblique incidence. J Acoust Soc Am 1997;102 (4):2200–10.
[15] Alvarez J, Jacobsen F. In-situ measurements of the complex acoustic impedance of porous materials. In Proc. of Internoise 2007, Istanbul, Turkey; 2007.
[16] Brandão E, Mareze P, Lenzi A, Da Silva AR. Impedance measurement of non-locally reactive samples and the influence of the assumption of local reaction. J Acoust Soc Am 133.
[17] Hirosawa K, Nakagawa H, Kon M, Yamamoto A. Investigation of absorption coefficient measurement of acoustical materials by boundary element method using particle velocity and sound pressure sensor in free field. Acoust Sci Technol 2009;30(6):442–5.
[18] Miki Y. Acoustical properties of porous materials – Generalizations of empirical models –. J Acoust Soc Jpn (E) 1990;11(1):25–8.
[19] Brandão E, Lenzi A, Cordioli J. Estimation and minimization of errors caused by sample size effect in the measurement of the normal absorption coefficient of a locally reactive surface. Appl Acoust 2012;73(6–7):543–56.
[20] Garai M, Guidorzi P. European methodology for testing the airborne sound insulation characteristics of noise barriers in situ: Experimental verification and comparison with laboratory data. J Acoust Soc Am 2000;108(3):1054.
[21] Alvarez JDB, Jacobsen F. In-situ measurements of the complex acoustic impedance of porous materials. In Proceedings of the 36th International Congress and Exhibition on Noise Control Engineering (Inter-Noise): 2007 Aug 28–31; Istanbul, Turkey, vol. 6; 2007. pp. 4308–4317.
[22] Brandão E, Tijs E, Lenzi A, de Bree H-E. A comparison of three methods to calculate the surface impedance and absorption coefficient from measurements under free field or in situ conditions. Acta Acust United Acust 2011;97:1025–1033.